How to cite: *Angew. Chem. Int. Ed.* **2020**, *59*, 9514–9521
International Edition: doi.org/10.1002/anie.201916281
German Edition: doi.org/10.1002/ange.201916281

DNA Motors

Tunable DNA Origami Motors Translocate Ballistically Over µm Distances at nm/s Speeds

Alisina Bazrafshan, Travis A. Meyer, Hanquan Su, Joshua M. Brockman, Aaron T. Blanchard, Selma Piranej, Yuxin Duan, Yonggang Ke, and Khalid Salaita**

Abstract: *Inspired by biological motor proteins, that efficiently convert chemical fuel to unidirectional motion, there has been considerable interest in developing synthetic analogues. Among the synthetic motors created thus far, DNA motors that undertake discrete steps on RNA tracks have shown the greatest promise. Nonetheless, DNA nanomotors lack intrinsic directionality, are low speed and take a limited number of steps prior to stalling or dissociation. Herein, we report the first example of a highly tunable DNA origami motor that moves linearly over micron distances at an average speed of 40 nm/min. Importantly, nanomotors move unidirectionally without intervention through an external force field or a patterned track. Because DNA origami enables precise testing of nanoscale structure-function relationships, we were able to experimentally study the role of motor shape, chassis flexibility, leg distribution, and total number of legs in tuning performance. An anisotropic rigid chassis coupled with a high density of legs maximizes nanomotor speed and endurance.*

Introduction

Biological motor proteins that convert chemical energy into controlled nanomechanical motion are essential and shared among all branches of life.[1] For example, the kinesin, myosin and dynein superfamily of molecular motors are critical for neuronal function and survival.[2] Motor proteins such as kinesin harness the chemical energy stored in adenosine triphosphate to autonomously take unidirectional mechanical steps at speeds of 20–200 nm/s.[3] Over the past two decades, there has been considerable interest in developing synthetic nanomotors[4] that recapitulate the properties of their biological counterparts. Such motors hold promise in biosensing,[5] molecular computing,[6] creating synthetic cells,[7] and drug delivery.[8]

Nanoscale machines constructed using DNA have shown great promise because of the well understood kinetics, thermodynamics, and structural predictability of Watson–Crick base pairing.[9] Autonomous[10] and non-autonomous[11] DNA motors, as well as diffusional DNA walking devices[12] have been reported to perform a variety of tasks, including cargo sorting[12b] and transport,[13] RNA sensing[5,10a] and mechanical bond rupture.[14] DNA nanomotors break the symmetry required for directed motion at low Reynolds number[15] using a mechanism known as a burnt-bridge Brownian ratchet (BBR).[16] This mechanism involves binding to a "foothold" site, followed by a transformation step (hydrolysis, displacement, etc.) that diminishes affinity to the occupied foothold, hence breaking symmetry and biasing motion to an adjacent unoccupied foothold site.

Despite engineering advances, DNA-based BBR motors suffer from limited processivity, low velocity, and lack of directionality. Polyvalent DNA motors (that incorporate more than two DNA legs) demonstrate improved processivity but diminished speed due to uncoordinated motion of individual DNA legs.[13,17] Most unipedal and bipedal walkers can only take a limited number of steps total.[17b,18] Speed can be sacrificed in exchange for enhanced processivity as was demonstrated by Ellington and colleagues by using a "cleat" to enhance the processivity of a unipedal walker from 36[10a] to 47[19] steps. Alternatively, Nir et al. sacrificed autonomy of bipedal DNA walkers to gain processivity, increasing the number of steps from 7[20] to 32 (44% percent of the walkers).[21] Increasing the number of DNA legs to create polyvalent DNA motors can also boost processivity at the cost of diminished speed. Lund et al.'s molecular spider[17a] comprised of 3 legs, can take upto 50 steps to traverse 100 nm over the course of hours. Similarly, quantum dots with 10–30 DNA legs can move along carbon nanotube tracks, translocating 2 µm over 12 h.[22] The low speeds are ultimately due to the lack of coordination of legs which result in unproductive track interactions. These experiments are supported by theory showing a trade-off between motor processivity (endurance) and speed.[23] Meaning, increasing polyvalency, increases motor speed at a cost of decreasing velocity. Herein, we address this fundamental trade-off by harnessing the DNA origami technique to identify the critical parameters enabling a polyvalent nanoscale BBR DNA motor that rolls to exhibit rapid (nm/s), processive (µm distances) and unidirectional motion.

DNA origami is a powerful method to construct three-dimensional structures with nanometer precision.[24] DNA origami has been instrumental in the field of dynamic DNA nanotechnology. In fact, the vast majority of DNA motors use DNA origami as their track.[17a,20a,21,25] Patterning the location

[*] A. Bazrafshan, H. Su, S. Piranej, Y. Duan, Y. Ke, K. Salaita
Department of Chemistry, Emory University
1515 Dickey Drive, Atlanta, GA 30322 (USA)
E-mail: yonggang.ke@emory.edu
ksalaita@emory.edu
T. A. Meyer, J. M. Brockman, A. T. Blanchard, Y. Ke, K. Salaita
Wallace H. Coulter Department of Biomedical Engineering, Georgia Institute of Technology and Emory University
Atlanta, GA 30322 (USA)
Supporting information and the ORCID identification number(s) for the author(s) of this article can be found under https://doi.org/10.1002/anie.201916281.

of fuel footholds on an origami scaffold is also a common strategy to guide motor trajectory.[12b,17a,20a,21,26] Herein, we aimed to test the hypothesis that DNA origami structures can be engineered as the body for a polyvalent DNA motor. The premise is that DNA origami enables exploring parameters such as leg density, distribution, and the role of body rigidity to identify the guidelines for optimal motor design. To our knowledge, our work represents the first example of a DNA origami nanomotor that processively converts chemical fuel into sustained mechanical motion (Table S1). Note that prior work in dynamic DNA origami employed multistate switches,[27] and are not motors processively converting chemical energy into mechanical work.[4e,28]

Results and Discussion

Inspired by our previous finding that structurally anisotropic microscale motors exhibit unidirectional motion,[10b] we created a DNA origami motor consisting of a bundle of 16 DNA double helices (16HB) linked together to produce a rectangular prism with dimensions ca. 10 nm × 10 nm × 130 nm (Figure 1). The 16HB structure was assembled by annealing a mixture of short synthetic "staple strands" with a long "scaffold" strand and its structure confirmed using TEM (Figure 1, S1–S2, Table S2–S4). We engineered 36 DNA legs on each face of the rectangular prism (total = 144) with sequences complementary to a single-stranded RNA (ssRNA) monolayer which provided foothold sites (Figure 1 a,b,c, S3,S4). RNA footholds were tagged with Cy3, enabling visualization of RNA hydrolysis during BBR translocation. Additionally, we loaded 8 cargo-binding DNA strands at each end of the 16HB (total = 16 cargo-binding strands) with AF647-tagged oligos, enabling tracking of 16HB motor motion using fluorescence microscopy.

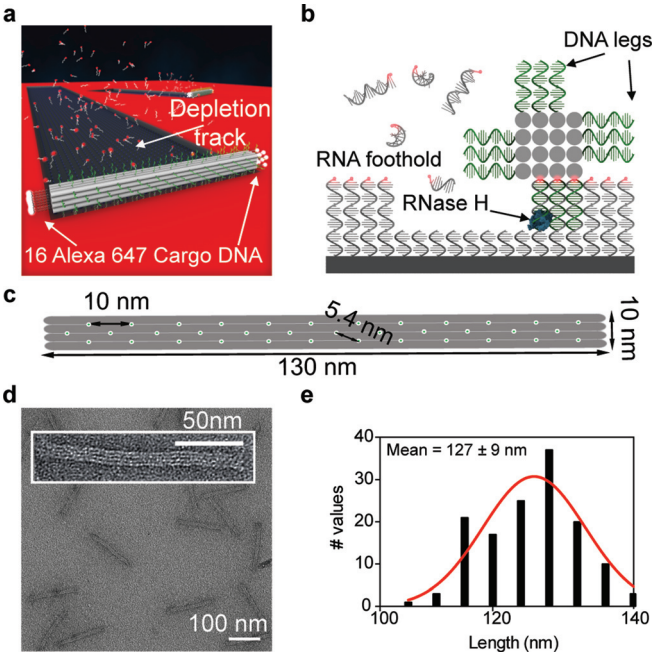

Figure 1. Design of 16 helix bundle (16HB) nanoscale motor: a) Schematic drawing showing 16HB motor motion. b) Side view of the motor highlighting the enzymatically driven mechanism of motion. RNase H exclusively cleaves RNA hybridized to the DNA legs but not single stranded RNA. c) Top view of 16HB showing location of DNA legs (green dot with white border). Note that this leg placement is repeated on each of the four long faces of the 16HB. d) TEM image of 16HB. e) Histogram of 16HB lengths measured from TEM. $n = 137$ origami structures that were synthesized from two different synthesis batches.

Introduction of DNA origami motors (10 pM) to the RNA monolayer led to motor binding within minutes (Supplementary movie 1 and Figure S5). Motors remained immobile due to DNA-RNA hybridization. Upon addition of RNase H (an enzyme that selectively cleaves RNA that is duplexed, but not ssRNA), single-particle fluorescence tracking revealed motor translocation across the surface (Figure 2 a,b, Supplementary movies 2 and 3). The motion of the nanomotors coincided with loss of the Cy3-tagged RNA footholds (56 % loss, Figure S6), which exclusively occurred upon addition of RNase H (Figure 2 a). Quantitative analysis of a subset of nanomotor x–y trajectories showed that motion was linear (Figure 2 b shows the trajectory of a single motor). This linearity was validated by plotting the mean square displacement (MSD) of nanomotors over time, revealing a power law relation with an exponent of 1.92 (Figure 2 c). Note that MSD is proportional to $time^{\alpha}$, where α is a scaling factor that is 1 for random (Brownian) diffusion, <1 for sub-diffusive motion, and >1 for super-diffusive motion.[29] In this case, $\alpha = 1.92$, indicating highly ballistic (linear) motion. Figure 2 d shows $n = 33$ trajectories overlaid with the origin as the start position. Trajectory lengths were negligible when RNase H was withheld, thus validating the track analysis routine and the role of RNase H in driving motion (Figure 2 e and Figure S7). Using the *Picasso* single molecule localization software[30] along with smoothing[31] and drift correction algorithms and custom MATLAB scripts, we analyzed the trajectories of hundreds of motors in an automated manner (Figure S8 and S9). Analyses of 173 motors showed that motor speed increased with increasing concentrations of enzyme, showing that fuel consumption rate tunes the translocation rate (Figure 2 f and Figure S10). 97 % of trajectories are super-diffusive ($\alpha > 1.0$) and a significant fraction of trajectories were linear as the ensemble showed $\alpha = 1.7 \pm 0.3$ (Figure 2 g). Although nanomotor speed is tuned by enzyme concentration, motors always moved linearly, as reflected by their α coefficient. Enzyme concentrations greater than 43.2 nM did not show any further enhancement in speed and instead reduced processivity due to motor dissociation from the surface as demonstrated by quantifying the percent of motors bound to the surface as a function of time (Figure 2 h). At 43.2 nM RNase H, 80 % of motors remain bound on the track at $t = 60$ min (Figure 2 h), and in this population, the average net displacement and the average total displacement were 560 ± 220 nm and 1320 ± 460 nm, respectively.

We further investigated the role of formamide, and found that increasing the concentration of this denaturant increases net displacement (motor speed, Figure 2 i). This result is consistent with our observation that formamide increases the RNase H hydrolysis rate (Figure S11). Moreover, denaturants will also dampen unproductive interactions between DNA

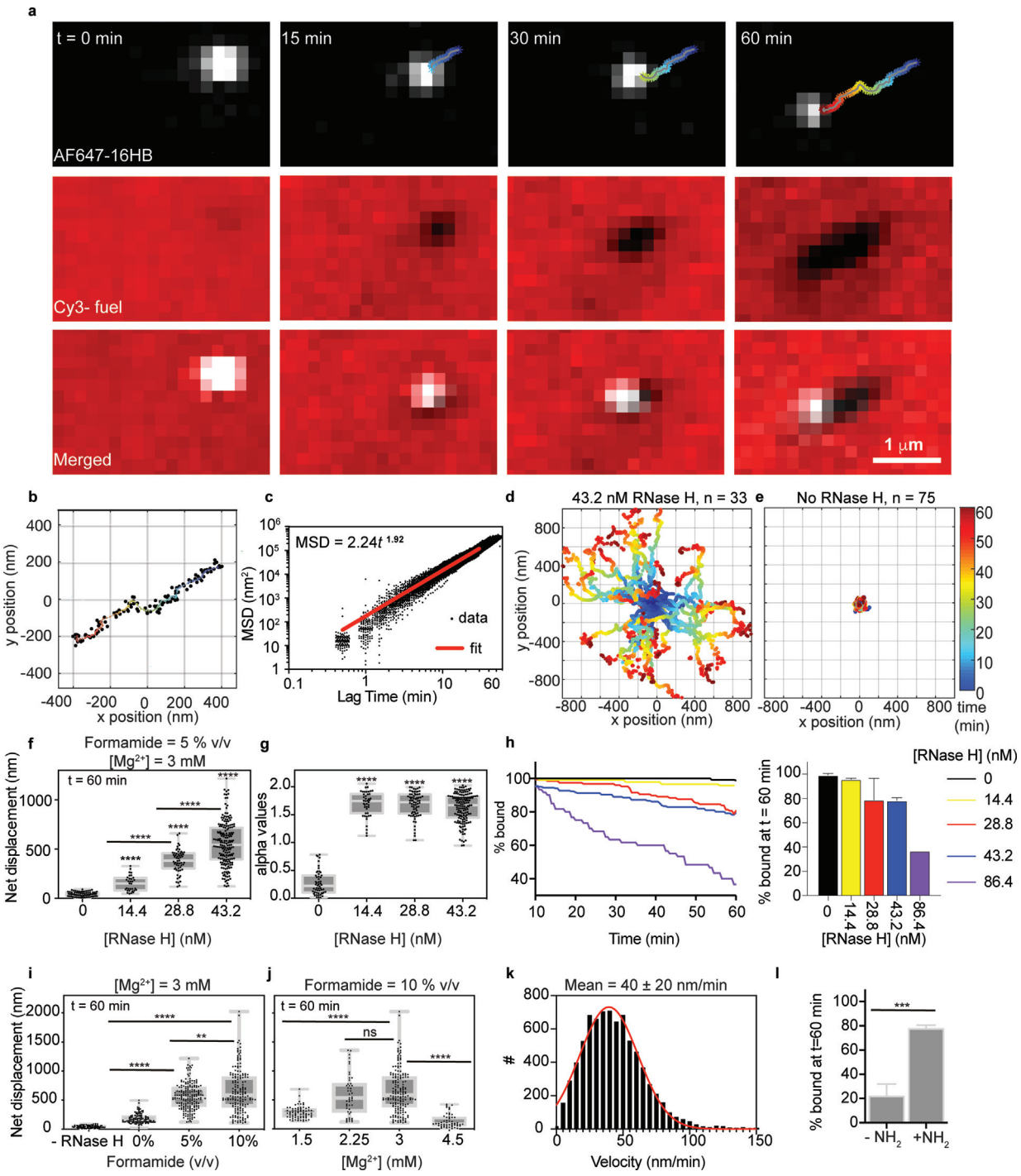

Figure 2. 16 HB DNA origami functions as a motor: a) Time-lapse fluorescence images of A647-16HB, Cy3-fuel, and overlay of a single motor. Colored line shows motor trajectory (60 min), color bar is the same as (d). b) AF647-16HB localizations (black dots) and smoothed trajectory (colored line). c) Plot of MSD as a function of time for motor in (a), providing the alpha value. d) Ensemble of motor trajectories ($n=33$) with 43.2 nM RNaseH and e) without RNaseH. f) Plot of motor net displacement and g) alpha value as a function of enzyme concentration. Each dot represents a single motor, box represents 95% CI with median, and the bars represent the min and max of ($n=98$, 27, 59 and 173 for 0, 14.4, 28.8 and 43.2 nM respectively generated from two (14.4 nM) or three (negative control, 28.8 and 43.2 nM) independent experiments). **** indicates that $p<0.0001$. h) Plot of percentage of motors bound to surface as a function of time for different enzyme concentrations (left) and percent of motor bound at the end of a one-hour acquisition (right). Error bars represent the standard deviation from two (14.4 nM) or three (negative control, 28.8 and 43.2 nM) independent experiments. The 86.6 nM group was tested on one surface for 60 minutes. i) Plot of motor net displacement at $t=60$ min as a function of formamide concentration and j) Mg^{2+} concentration. Each dot represents a single motor, box represents 95% CI with median, and the bars represent the min and max of ($n=98$, 111, 173 and 154 for -RNase H, 0%, 5% and 10% formamide, respectively generated from three independent experiments and $n=70$, 47, 154 and 51 for 1.5, 2.25, 3 and 4.5 mM Mg^{2+} respectively generated from one(1.5, 2.25, 4.5 mM) and three (3 mM) experiments. **** indicates that $p<0.0001$ and ** indicates $p=0.0015$. k) Histogram of instantaneous velocities of $n=99$ origami motors. l) Plot comparing the role of amine modified anchor in processivity of 16HB motors. Error bars represent the standard deviation in % motors bound at $t=60$ min for three independent experiments. *** indicates $p=0.0006$.

legs and depleted track which will also increase motor speed.[32] However, we observed RNA fuel degradation at the 10% formamide concentration, which is likely due to the disassembly of the DNA origami structure and release of DNA legs. Indeed, we confirmed that 16HB is stable in 5% formamide and 3 mM Mg^{2+} (Figure S12). 3 mM Mg^{2+} produced optimal motor speed (Figure 2j), which is likely a compromise between maximizing the k_{cat} of RNaseH and stabilization of 16HB interactions to the surface.

A histogram of instantaneous velocity ($\Delta t = 30$ s) of $n = 99$ 16HB motors shows that the mean velocity was 40 nm/min (10% formamide, 3 mM Mg^{2+}) which is the fastest DNA nanomotor reported to date. Furthermore, a small subset of the motors reached speeds above 100 nm/min. Velocity histograms of individual motors showed that this range of behaviours was not unique to a specific subset of motors and rather all motors showed a wide range of instantaneous velocities (Figure S9). By happenstance, we found that incorporation of a 5′ terminal primary amine in the DNA anchor (Table S2) produced enhanced processivity (Figure 21). While control experiments demonstrate that 16HB motors are exclusively bound to the surface only when the RNA fuel is complementary to the DNA legs (Figure S5). This result suggests an important role for the amine in screening repulsive interactions and optimizing motor-surface binding.

To confirm the importance of having an anisotropic chassis in mediating linear motion, we synthesized spherical DNA motors with a diameter of 50 nm (Figure S13 and Supplementary Movie 4). As expected, these spherical motors moved in an RNase H-dependent manner with $\alpha = 1.45 \pm 0.22$, which is super-diffusive and consistent with self-avoiding motion. This result confirms that the anisotropic shape of the 16HB is critical for achieving unidirectionality.

Because there is no precedent for a DNA nanomotor that intrinsically moves in a unidirectional manner, we validated the result using two additional lines of evidence. The first was based on super-resolution imaging of the Cy3 depeletion track widths (Figure 3a,b and S14). Structured illumination microscopy (SIM)[33] showed that the width of track depletion

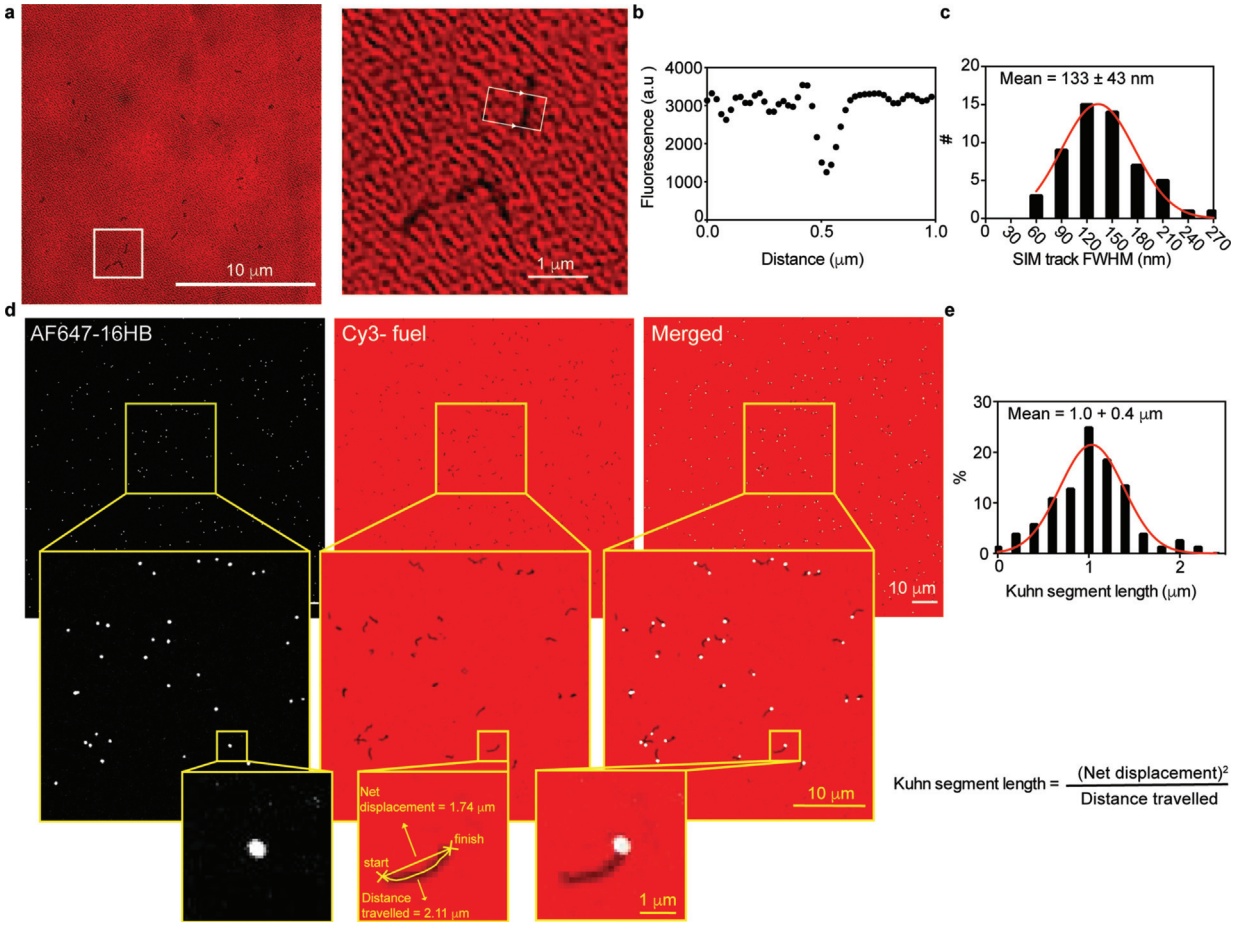

Figure 3. Depletion track analysis indicates linear motion orthogonal to 16HB long axis: a) A representative SIM image of Cy3-fuel depleted tracks. A line scan with width of 10 pixels was drawn perpendicular to the track (arrowed box, the direction of arrows shows direction of *x* axis of linescan) to measure the width of the depleted track. b) Representative linescan profile of the linescan shown in (a). c) Histogram of full width at half maximum (FWHM) of 56 tracks. FWHM are calculated by fitting the normalized inverted fluorescence values to a Gaussian function. The mean of the FWHM of 56 tracks was 133 ± 43 nm as determined using a Gaussian fit to the data. d) Fluorescence images of A647-16HB, Cy3-fuel, and overlay at time = 90 min. Insets show zoom-in of single particle track as well as an example of how net displacement and distance travelled were measured. e) Histogram of Kuhn segment length obtained from analysis of $n = 158$ depletion tracks obtained from three different experiments. A Gaussian fit to the histogram of Kuhn segment lengths shows a mean = 1.0 ± 0.4 μm.

was 133 ± 43 nm (Figure 3c, Figure S14), which matched the length of the nanomotor (127 ± 9 nm) based on TEM analysis (Figure 1d). This shows that nanomotors move in an orientation orthoganol to their long axis. The second line of evidence comes from quantifying the linearity of nanomotor-generated depletion tracks, which displayed a Kuhn segment length of 1.0 ± 0.4 μm (Figure 3d,e and S15).This indicates that nanomotors moved ≈100 body lengths before changing direction, which may be due to surface imperfections, nanomotor defects, and partial track dissociation. Taken together, 16HB DNA origami motors move processively and linearly likely via a rolling mechanism where the motor pivots from one face to an adjacent face of the structure.

To confirm that the mechanism of translocation is indeed face-over-face rolling and not walking/sliding along a single face, we created a library of origami structures with anisotropic display of DNA legs across the four faces of the rectangular prism. We describe these structures as "geometric mutations" of the 16HB parent motor. Specifically, we created geometric mutations presenting legs on one (1–36), two (2_{trans}-36; 2_{cis}-36), three (3–36), and four faces (4–36) of the rod (Figure 4a and S16). If motion primarily occurs through rolling, then we would expect diminished translocation for nanomotors with missing legs on specific faces due to hindrance in rolling. The 1-36 and 2_{cis}-36 showed diminished net displacements (≈46% reduction in displacement) along with $\alpha = 1.19 \pm 0.36$ (1-36) and 1.15 ± 0.41 (2_{cis}-36), demonstrating loss of linear motion. Random motion is consistent with the behavior of DNA bi-pedal diffusive motors when placed on a 2D track surface.[12a] The 3-36 geometric mutation showed intermediate net displacements (470 ± 189 nm) and α coefficients (1.39 ± 0.32) suggesting motion that was in-between that of the diffusive walkers and the rolling motors. Finally, the 2_{trans}-36 motors translocate with displacements and α values that were not distinguishable from that of the 4-36 motors (Figure 4b,d,e). This data set shows that nanomotor rolling is enhanced when either all four faces or when two opposing faces present DNA legs. This may suggest that symmetry aids in rolling. Conversely, the three-face motors are somehow hindered from rolling due to possible back-face interactions with the depleted track as only 56% of the RNA is cleaved (Figure S6).

To resolve the difference between diffusive 2D walking/sliding and rolling we withheld formamide from the solution to further enhance the non-productive interactions between DNA legs and depleted track. Removing formamide also

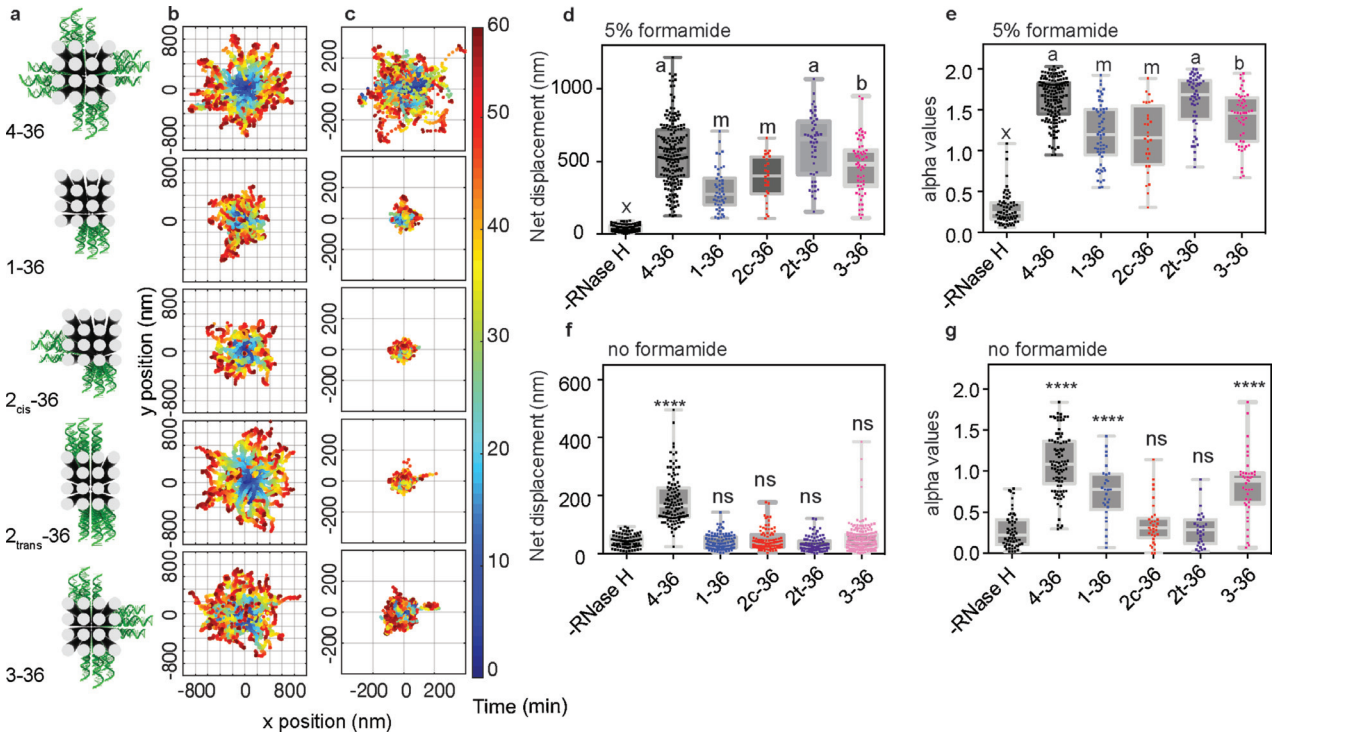

Figure 4. Geometric mutations show that 16HB origami motors move by rolling: a) Schematic showing the library of geometric mutants tested. b) Ensemble trajectories of different motors with and c) without the addition of 5% (v/v) formamide. d) Plots of net displacement and e) alpha values for motors shown in (e). Each dot represents a single motor, box represents 95% CI with median, and the bars represent the min and max (n = 98, 173, 46, 26, 49, and 61 for negative control, 4-36, 1-36, 2c-36, 2t-36 and 3-36 generated from two (2c-36 and 2t-36) or three (negative control, 4-36, 1-36 and 3-36) independent experiments). a, b, m, x indicate not statistically significant and $p < 0.1$, $p < 0.01$ and $p < 0.0001$ respectively, in comparison to the positive control. f,g) plots similar to the ones in (d) and (e) but withholding formamide (n = 77, 152, 112, 94, 92 and 167 for negative control, 4-36, 1-36, 2c-36, 2t-36 and 3-36 respectively generated from three independent experiments. **** indicates $p < 0.0001$ compared to the negative control. Note that plot of alpha value has a lower n as the $R^2 < 0.9$ of the log–log fit for a some of the stalled trajectories).

slowed RNase H hydrolysis three-fold (Figure 2i and Figure S11), further increasing the barrier to motor translocation. Under these stringent conditions, only the 4–36 nanomotors moved; deleting DNA legs from any of the motor faces led to complete stalling (Figure 4c,f,g). Thus, motors primarily translocate by rolling when all four faces display DNA legs. Walking-based motion is allowed, but this mode of transport is less efficient, more diffusive, and weakly processive; and hence stalls when presented with barriers. Chemomechanical modeling of motor transport along a 1D track shows that motors can toggle between walking and rolling as a function of enzymatic hydrolysis rate and dissociation rate from footholds (Figures S17–S19). Importantly, the models predict that withholding formamide leads to a transition from rolling/walking to obligatory rolling in agreement with our experimental results.

We next hypothesized that the efficient motion depends on a rigid chassis. We created more flexible motors by intentionally creating single stranded regions within the middle of the motor chassis. Specifically, we removed 8 nt (Δ8) and 32 nt (Δ32) segments of a subset of the staples in the 16HB (Figure 5a, S20 and S21). TEM was used to quantify the flexibility of parent 16HBs as well as the Δ8 and Δ32 mutants (Figure 5b,c and S21). As expected, the Δ32 showed the greatest flexibility which was followed by the Δ8 and the parent 16HB. Using single particle localization analysis (Figure 5d), we found that the increasing chassis flexibility leads to a significant reduction in the net displacement (50% and 55% for Δ8 and Δ32 respectively) accompanied with a decrease in the linearity of the motion (Figure 5e,f). Indeed, the Δ8 and Δ32 motors displayed an $\alpha = 1.40 \pm 0.28$ and 1.23 ± 0.41, respectively. Therefore, achieving linear motion requires a rigid motor chassis, which allows for mechanical communication or coordination between the legs of the motor.

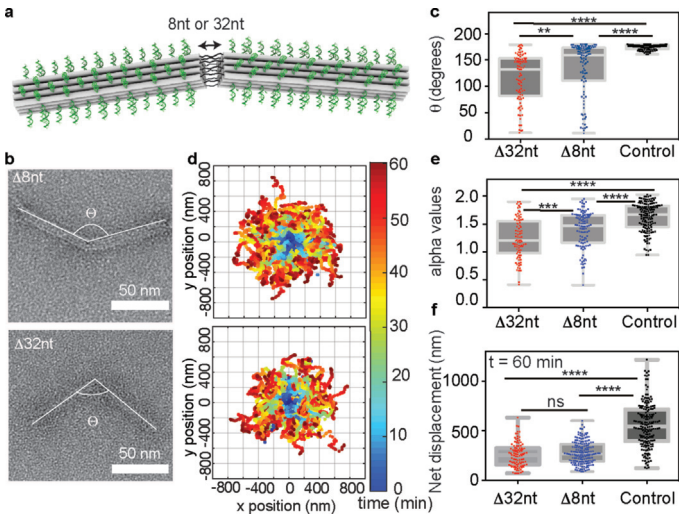

Figure 5. A rigid chassis is necessary for linear motion: a) Schematic showing how motor rigidity was tuned. b) TEM images of Δ8 and Δ32 motors that were used to determine the angle Θ as a measure of rigidity. c) Plots showing α for control, Δ8 and Δ32 motors. (n = 100,100 and 89 for control, Δ8 and Δ32 respectively). d) Trajectories of Δ8 and Δ32 motors. e) Plots of alpha values and f) net displacements for Δ8 and Δ32 and control motors. Each dot represents a single motor, box represents 95% CI with median, and the bars represent the min and max of (n = 110, 85, and 173 for Δ8, Δ32 and control, respectively generated from three independent experiments). **, *** and **** and ns indicate $p = 0.0059$, $p = 0.0006$, $p < 0.0001$ and not statistically different, respectively.

Another important parameter that likely controls the speed and directionality of motors is the number and distribution of DNA legs. To test this, we created a series of DNA origami structures with different leg numbers and distribution (Figure 6, S22 and S23). First, we reduced the density of DNA legs to 12 and 24 strands on each face (Figure 6a). We initially anticipated that reducing the density of DNA legs would lead to an enhancement in motor speed, because each step would require fewer cleavage events. To our surprise, we found that reducing leg density led to a significant decrease in motor speed ($\approx$25% and $\approx$43% decrease in speed for the 24 and 12 DNA legs/face structures, respectively, Figure 6b,c). These motors likely still moved by rolling, as there was no significant change in α values (Figure 6g). Furthermore, quantification of RNA hydrolysis in depleted tracks demonstrated that 12 and 24 leg/face samples consumed the same fraction of RNA (Figure S24). The conclusion was maintained when we withheld formamide, and motors with 12 legs/face were stalled (Figure S25). Therefore, increasing DNA leg density accelerates motor speed. As further evidence supporting this trend, we found that nanoparticles displaying greater densities of DNA (1 DNA/5 nm^2) reach instantaneous velocities up to 2.5 μm/min in optimized conditions (Figure S13). Motors with half the total number of DNA legs (18 on each face) but presented at the same density moved just as rapidly as the 36 DNA legs/face control group (Figure 6d,e,f). These trends were also reproduced upon withholding formamide (Figure S26). An exception to this general rule appears when DNA density is maintained but leg distribution is not uniform. For example, separating legs into two groups of 9 and 9 that are 60 nm apart, resulted in a 35% decrease in net displacement coupled with a decrease in α (Figure 6g). Given that the 9 + 9 motors moved a total distance that was on par with the 4–36 motor (Figure S27), this suggested that the structure is more prone to direction changes compared to the 18 DNA legs/face motors. Accordingly, we speculate that placing DNA legs at separate domains increases diffusive behaviour, reducing α due to a number of factors that include surface and motor heterogeneity.

Conclusion

This new class of origami motors demonstrate autonomous unidirectional motion over distances of multiple microns without the guidance of an external magnetic, chemical or electrochemical gradient. Motors carry many copies of DNA cargo with instantaneous velocities of up to 100 nm/min which, to our knowledge, represents the fastest and most processive nanoscale DNA motor reported to date. We show a polyvalent BBR-based DNA motor that rolls and undertakes processive linear steps, and thus resembles the

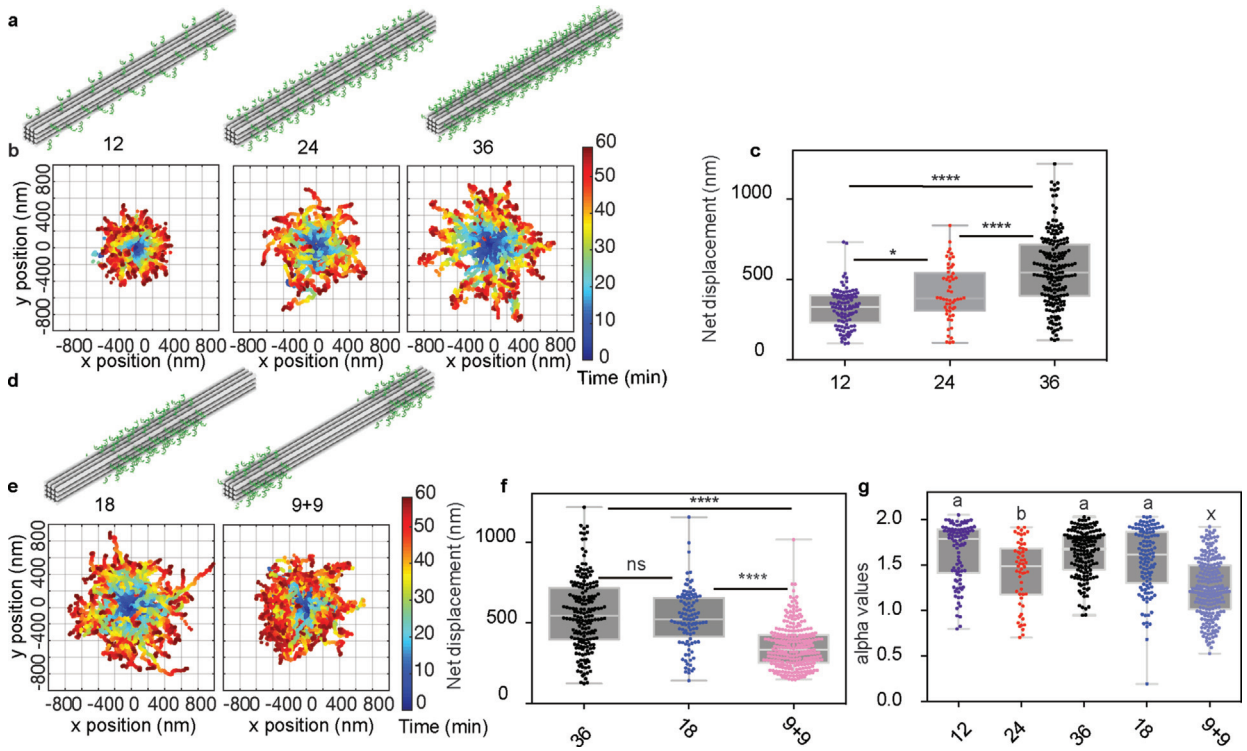

Figure 6. Leg density and not the absolute number of legs enhances motor speed: a) Schematic of motors with different leg densities: 12, 24 and 36 legs/face. b) Trajectories of motors with different leg densities. c) Plot of net displacement for motors with 12, 24, and 36 legs/face. d) Schematic design of 16HB 18 and 9+9. The density of the DNA legs is similar to 16HB-36. e) Trajectories from a representative experiment are plotted below each structure. f) Plots of net displacements for motors 18, 9+9 and 36. g) Plot of alpha values for motors 12, 24, 36, 18 and 9+9. Each dot represents a single motor, box represents 95% CI with median, and the bars represent the min and max of (n=93, 55, 173, 116 and 214 for 12, 24, 36, 18 and 9+9 respectively generated from three independent experiments). *, **** and ns indicate p=0.0181, p<0.0001 and not statistically different. a, b, x indicate not statistically significant, p=0.0034 and p<0.0001, respectively, in comparison to the positive control.

behaviour of biological motor proteins despite operating with a completely different mechanism. Rapid ballistic and processive movement requires high leg density with a symmetrical leg distribution that is coupled to a rigid and rod-shaped chassis. This work highlights the power of the DNA origami technique to systematically test structure-function relationships at the nanoscale thus uncovering the design principles for programming autonomous motion with specific diffusive properties.

We recognize that the 16HB likely displays a global twist, however the spacers engineered in the RNA fuel as well as the DNA anchor and the DNA legs all help to minimize the impact of this twist. Our work represents the tip of the iceberg in terms of fully exploring the structural parameters that tune and optimize motor performance. In addition to the parameters explored here, one can envision important roles for chassis shape, aspect ratio, leg flexibility and span, and the free energy of hybridization between the legs and the fuel. Indeed, theoretical modelling by Forde and colleagues predicts massive enhancement in motor performance as a function of optimizing polyvalency and leg span.[23a] Moreover, sequence optimization will also further tune the kinetics of hybridization as was recently shown in the speed-optimized DNA PAINT.[34] We anticipate future theoretical and experimental work using DNA origami motors to explore these parameters and further advance the field of synthetic motors. We acknowledge that these synthetic DNA motors have significant room for improvement to recapitulate the properties of biological motors in terms of energy conversion efficiency, speed, and processivity. Nonetheless, this work takes an important step toward realizing these future objectives.

Acknowledgements

We thank Stephanie Jones (https://bio-illustration.com/) for her artwork demonstrating the Scheme in Figure 1 and Dr. Justin Burton to allow access to use the laser cutter in his lab. We also acknowledge support from NSF 1611102, NSH DMR 1905947, NIH R01 GM124472 and NSF CAREER 1350829 (K.S), NSF DMR 1654485 and ECCS-1807568, NIH grant 1R21AI135753-01, and Semiconductor Research Corporation (SRC) grant 2836.002 (Y.K.) and NSF GRFP DGE-1444932 (A.T.B.). Furthermore, we acknowledge the support from Robert P. Apkarian Integrated Electron Microscopy Core and Emory University Integrated Cellular Imaging Microscopy Core.

Conflict of interest

The authors declare no conflict of interest.

Keywords: DNA motors · DNA origami · dynamic DNA nanotechnology · fluorescence microscopy · nanomachines

[1] M. von Delius, D. A. Leigh, *Chem. Soc. Rev.* **2011**, *40*, 3656 – 3676.
[2] N. Hirokawa, S. Niwa, Y. Tanaka, *Neuron* **2010**, *68*, 610 – 638.
[3] R. D. Vale, T. Funatsu, D. W. Pierce, L. Romberg, Y. Harada, T. Yanagida, *Nature* **1996**, *380*, 451.
[4] a) W. F. Paxton, K. C. Kistler, C. C. Olmeda, A. Sen, S. K. St. Angelo, Y. Cao, T. E. Mallouk, P. E. Lammert, V. H. Crespi, *J. Am. Chem. Soc.* **2004**, *126*, 13424 – 13431; b) K. K. Dey, X. Zhao, B. M. Tansi, W. J. Méndez-Ortiz, U. M. Córdova-Figueroa, R. Golestanian, A. Sen, *Nano Lett.* **2015**, *15*, 8311 – 8315; c) D. A. Wilson, R. J. M. Nolte, J. C. M. v. Hest, *Nat. Chem.* **2012**, *4*, 268 – 274; d) S. Sengupta, K. K. Dey, H. S. Muddana, T. Tabouillot, M. E. Ibele, P. J. Butler, A. Sen, *J. Am. Chem. Soc.* **2013**, *135*, 1406 – 1414; e) P. Zhan, M. J. Urban, S. Both, X. Duan, A. Kuzyk, T. Weiss, N. Liu, *Sci. Adv.* **2019**, *5*, eaax6023; f) M. R. Wilson, J. Solà, A. Carlone, S. M. Goldup, N. Lebrasseur, D. A. Leigh, *Nature* **2016**, *534*, 235 – 240.
[5] H. Peng, X.-F. Li, H. Zhang, X. C. Le, *Nat. Commun.* **2017**, *8*, 14378.
[6] A. Credi, V. Balzani, S. J. Langford, J. F. Stoddart, *J. Am. Chem. Soc.* **1997**, *119*, 2679 – 2681.
[7] a) J. Pan, Y. Du, H. Qiu, L. R. Upton, F. Li, J. H. Choi, *Nano Lett.* **2019**, *19*, 9138 – 9144; b) A. Somasundar, S. Ghosh, F. Mohajerani, L. N. Massenburg, T. Yang, P. S. Cremer, D. Velegol, A. Sen, *Nat. Nanotechnol.* **2019**, *14*, 1129 – 1134.
[8] M. Wegener, M. J. Hansen, A. J. M. Driessen, W. Szymanski, B. L. Feringa, *J. Am. Chem. Soc.* **2017**, *139*, 17979 – 17986.
[9] A. Blanchard, K. Salaita, *Science* **2019**, *365*, 1080.
[10] a) C. Jung, P. B. Allen, A. D. Ellington, *Nat. Nanotechnol.* **2016**, *11*, 157 – 163; b) K. Yehl, A. Mugler, S. Vivek, Y. Liu, Y. Zhang, M. Fan, E. R. Weeks, K. Salaita, *Nat. Nanotechnol.* **2016**, *11*, 184 – 190.
[11] J.-S. Shin, N. A. Pierce, *J. Am. Chem. Soc.* **2004**, *126*, 10834 – 10835.
[12] a) J. Li, A. Johnson-Buck, Y. R. Yang, W. M. Shih, H. Yan, N. G. Walter, *Nat. Nanotechnol.* **2018**, *13*, 723 – 729; b) A. J. Thubagere, W. Li, R. F. Johnson, Z. Chen, S. Doroudi, Y. L. Lee, G. Izatt, S. Wittman, N. Srinivas, D. Woods, E. Winfree, L. Qian, *Science* **2017**, *357*, eaan6558.
[13] T.-G. Cha, J. Pan, H. Chen, J. Salgado, X. Li, C. Mao, J. H. Choi, *Nat. Nanotechnol.* **2014**, *9*, 39.
[14] A. Blanchard, A. Bazrafshan, J. Yi, J. T. Eisman, K. M. Yehl, T. Bian, A. Mugler, K. Salaita, *Nano Lett.* **2019**, *19*, 6977 – 6986.
[15] E. M. Purcell, *Am. J. Phys.* **1977**, *45*, 3 – 11.
[16] a) J. Mai, I. M. Sokolov, A. Blumen, *Phys. Rev. E* **2001**, *64*, 011102; b) J. Bath, S. J. Green, A. J. Turberfield, *Angew. Chem. Int. Ed.* **2005**, *44*, 4358 – 4361; *Angew. Chem.* **2005**, *117*, 4432 – 4435; c) C. S. Korosec, M. J. Zuckermann, N. R. Forde, *Phys. Rev. E* **2018**, *98*, 032114.
[17] a) K. Lund, A. J. Manzo, N. Dabby, N. Michelotti, A. Johnson-Buck, J. Nangreave, S. Taylor, R. Pei, M. N. Stojanovic, N. G. Walter, E. Winfree, H. Yan, *Nature* **2010**, *465*, 206 – 210; b) T. Omabegho, R. Sha, N. C. Seeman, *Science* **2009**, *324*, 67.
[18] J. Bath, S. J. Green, K. E. Allen, A. J. Turberfield, *Small* **2009**, *5*, 1513 – 1516.
[19] C. Jung, P. B. Allen, A. D. Ellington, *ACS Nano* **2017**, *11*, 8047 – 8054.
[20] a) T. E. Tomov, R. Tsukanov, M. Liber, R. Masoud, N. Plavner, E. Nir, *J. Am. Chem. Soc.* **2013**, *135*, 11935—11941; b) M. Liber, T. E. Tomov, R. Tsukanov, Y. Berger, E. Nir, *Small* **2015**, *11*, 568 – 575.
[21] T. E. Tomov, R. Tsukanov, Y. Glick, Y. Berger, M. Liber, D. Avrahami, D. Gerber, E. Nir, *ACS Nano* **2017**, *11*, 4002 – 4008.
[22] T.-G. Cha, J. Pan, H. Chen, J. Salgado, X. Li, C. Mao, J. H. Choi, *Nat. Nanotechnol.* **2014**, *9*, 39 – 43.
[23] a) C. S. Korosec, M. J. Zuckermann, N. R. Forde, *Phys. Rev. E* **2018**, *98*, 032114; b) L. Samii, H. Linke, M. J. Zuckermann, N. R. Forde, *Phys. Rev. E* **2010**, *81*, 021106; c) L. Samii, G. A. Blab, E. H. C. Bromley, H. Linke, P. M. G. Curmi, M. J. Zuckermann, N. R. Forde, *Phys. Rev. E* **2011**, *84*, 031111.
[24] a) P. W. K. Rothemund, *Nature* **2006**, *440*, 297 – 302; b) P. Wang, T. A. Meyer, V. Pan, P. K. Dutta, Y. Ke, *Chem* **2017**, *2*, 359 – 382.
[25] F. Wang, X. Zhang, X. Liu, C. Fan, Q. Li, *Small* **2019**, *15*, 1900013.
[26] a) C. Zhou, X. Duan, N. Liu, *Nat. Commun.* **2015**, *6*, 8102; b) H. Gu, J. Chao, S.-J. Xiao, N. C. Seeman, *Nature* **2010**, *465*, 202.
[27] a) E. M. Willner, Y. Kamada, Y. Suzuki, T. Emura, K. Hidaka, H. Dietz, H. Sugiyama, M. Endo, *Angew. Chem. Int. Ed.* **2017**, *56*, 15324 – 15328; *Angew. Chem.* **2017**, *129*, 15526 – 15530; b) J. Song, Z. Li, P. Wang, T. Meyer, C. Mao, Y. Ke, *Science* **2017**, *357*, eaan3377.
[28] S. Kassem, T. v. Leeuwen, A. S. Lubbe, M. R. Wilson, B. L. Feringa, D. A. Leigh, *Chem. Soc. Rev.* **2017**, *46*, 2592 – 2621.
[29] N. Gal, D. Lechtman-Goldstein, D. Weihs, *Rheol. Acta* **2013**, *52*, 425 – 443.
[30] J. Schnitzbauer, M. T. Strauss, T. Schlichthaerle, F. Schueder, R. Jungmann, *Nat. Protoc.* **2017**, *12*, 1198.
[31] N. Michelotti, C. de Silva, A. E. Johnson-Buck, A. J. Manzo, N. G. Walter, *Methods Enzymol.* **2010**, *475*, 121 – 148.
[32] R. D. Blake, S. G. Delcourt, *Nucleic Acids Res.* **1996**, *24*, 2095 – 2103.
[33] M. G. L. Gustafsson, *J. Microsc.* **2000**, *198*, 82 – 87.
[34] F. Schueder, J. Stein, F. Stehr, A. Auer, B. Sperl, M. T. Strauss, P. Schwille, R. Jungmann, *Nat. Methods* **2019**, *16*, 1101 – 1104.

Manuscript received: December 18, 2019
Accepted manuscript online: February 3, 2020
Version of record online: April 1, 2020

